LAWRENCE
LIVERMORE
NATIONAL
LABORATORY

LLNL-JRNL-671547

Using Multiple Secondary Fusion Products to Evaluate Fuel pR, Electron Temperature, and Mix in Deuterium-filled Implosions at the NIF

H. G. Rinderknecht, M. J. Rosenberg, A. B. Zylstra, B. Lahmann, F. H. Seguin, J. A. Frenje, C. K. Li, M. Gatu Johnson, R. D. Petrasso, L. F. Berzak Hopkins, J. A. Caggiano, L. Divol, E. P. Hartouni, R. Hatarik, S. P. Hatchett, S. LePape, A. J. Mackinnon, J. M. McNaney, N. B. Meezan, M. J. Moran, P. A. Bradley, J. L. Kline, S. Krasheninnikova, G. A. Kyrala, T. J. Murphy, M. J. Schmitt, I. L. Tregillis, S. H. Batha, J. P. Knauer, J. D. Kilkenny

May 28, 2015

Physics of Plasmas

Disclaimer

Using multiple secondary fusion products to evaluate fuel ρR, electron temperature, and mix in deuterium-filled implosions at the NIF

H.G. Rinderknecht, M.J. Rosenberg,[a)] A.B. Zylstra, B. Lahmann, F.H. Séguin, J.A. Frenje, C.K. Li, M. Gatu Johnson, and R.D. Petrasso
Plasma Science and Fusion Center, Massachusetts Institute of Technology, Cambridge, Massachusetts 02139
L. F. Berzak Hopkins, J. A. Caggiano, L. Divol, E. P. Hartouni, R. Hatarik, S. P. Hatchett, S. Le Pape, A. J. Mackinnon, J. M. McNaney, N. B. Meezan, and M. J. Moran
Lawrence Livermore National Laboratory, Livermore, California 94550
P. A. Bradley, J. L. Kline, N. S. Krasheninnikova, G. A. Kyrala, T. J. Murphy, M. J. Schmitt, I. L. Tregillis, and S. H. Batha
Los Alamos National Laboratory, Los Alamos, New Mexico 87545
J. P. Knauer
Laboratory for Laser Energetics, University of Rochester, Rochester, New York 14623
J. D. Kilkenny
General Atomics, San Diego, California 92121

In deuterium-filled ICF implosions, the secondary fusion processes D(^{3}He,p)^{4}He and D(T,n)^{4}He occur as the primary products (^{3}He and T) react in flight with thermal deuterons. In implosions with moderate fuel areal density ($\sim$ 5–100 mg/cm^2), the secondary D-^{3}He reaction saturates while the D-T reaction does not, and the combined information from these secondary products is used to constrain both the areal density and either the plasma electron temperature or changes in the composition due to mix of shell material into the fuel. The underlying theory of this technique is developed and applied to three classes of implosions on the National Ignition Facility: direct-drive exploding pushers, indirect-drive 1-shock and 2-shock implosions, and polar direct-drive implosions. In the 1- and 2-shock implosions, the electron temperature is inferred to be 0.67$\times$ and 0.33$\times$ the burn-averaged ion temperature, respectively. The inferred mixed mass in the polar direct-drive implosions is in agreement with measurements using alternative techniques.

I. INTRODUCTION

In inertial confinement fusion (ICF), lasers are used to compress fusion fuels, with the goal of generating a 'hotspot' in which fusion is initiated, surrounded by a cold, dense fuel mass which can support a propagating fusion burn wave.[1] Successful fusion ignition requires, among other considerations, areal density in the hotspot high enough that fusion products deposit their energy locally ($\rho R \sim 0.3$ g/cm^2), and preventing non-fuel ions from mixing into the hotspot, where they radiate energy and inhibit fusion burn.[2] The electron temperature (T_e) also plays a significant role in alpha heating of the hotspot: for temperatures up to a few keV, the fusion-generated alphas predominantly lose their energy through collisions with electrons, such that the rate of alpha stopping is governed by T_e and electron density.[3] Experimental study of the core temperature, areal density, and composition is critical to make progress towards ignition.[4]

Nuclear fusion products have been used extensively to study the behavior of the high energy-density plasmas generated in ICF implosions.[5–12] The high sensitivity of thermonuclear fusion yield rate to plasma ion temperature and density[13] makes the nuclear reaction histories and profiles valuable for studying the core plasma. In an ICF implosion filled with deuterium, fuel ions undergo the following fusion reactions:

$$\begin{aligned} D + D \ &\rightarrow T \quad (1.01\ \text{MeV}) \ + \ p \ (3.02\ \text{MeV}) \ (50\%), \\ &\rightarrow {}^3He \ (0.82\ \text{MeV}) \ + \ n \ (2.45\ \text{MeV}) \ (50\%). \end{aligned} \tag{1}$$

Additionally, the energetic reactant products ^{3}He and T are themselves fusion reactants, and can fuse in-flight with thermal deuterons as they transit and escape the fuel:[14–23]

$$\begin{aligned} T \ &(\leq 1.01\ \text{MeV}) + D \rightarrow \\ &\quad n(11.9\text{–}17.2\ \text{MeV}) + \alpha(6.7\text{–}1.4\ \text{MeV}), \\ {}^3He \ &(\leq 0.82\ \text{MeV}) + D \rightarrow \\ &\quad p(12.6\text{–}17.4\ \text{MeV}) + \alpha(6.6\text{–}1.7\ \text{MeV}). \end{aligned} \tag{2}$$

These processes are called secondary fusion reactions. The yield of secondary protons and neutrons from these reactions depends sensitively on the areal density of the fuel (ρR_{fuel}), the electron and ion temperature, and the plasma composition.[24] Secondary yields, which probe the entire fuel volume, therefore provide a unique view on these important properties of the final fuel assembly at bang time.

Secondary yields have been used to assess the density and temperature profiles of the imploded fuel at bang time[22, 23] on implosions at the OMEGA laser facility.[25] Assuming a clean deuterium fuel, implosions with low fuel areal density were found to produce consistent yields of secondary protons and neutrons for laser

[a)] Currently at the Laboratory for Laser Energetics

intensities of $\sim 6\times10^{14}$ W/cm^2. However, shots with intensity above 10^{15} W/cm^2 produced a yield of secondary neutrons consistent with a fuel ρR nearly double the value naively inferred from secondary protons.[23] Mix of shell material into the fuel was proposed as an explanation for this discrepancy. However, the difference between electron and ion temperature in the fuel was not taken into account, although these temperatures are not generally equal and the electron/ion thermalization time can be long compared to the implosion.[26, 27] Since electron temperature and fuel composition affect the plasma stopping power in similar ways, both must be considered when considering secondary fusion processes.

A technique for simultaneously analyzing both the secondary DT-neutron and D^{3}He-proton yields produced in deuterium-filled ICF implosions was developed to assess fuel ρR, electron temperature, and mix. In warm D_2-filled implosions with moderate fuel ρRs in the range 5–100 mg/cm^2, increased stopping power changes the ratio of secondary D^{3}He-proton yield to secondary DT-neutron yield, as will be shown in Section II. Both the fuel electron temperature and mixing of shell material into the fuel impact the fuel stopping power and can affect the ratios of secondary to primary yield and the ratio of secondary yields. By using the combined information of the secondary DT-neutron and secondary D^{3}He-proton yields, these important and difficult-to-measure properties of the fuel assembly are addressed in three classes of experiments at the NIF: direct-drive exploding pushers, indirect-drive 1- and 2-shock implosions, and polar-direct-drive mix experiments. This technique provides valuable information about the state of the core during peak nuclear production in experiments with D_2 fuel, which will be used to validate hydrodynamic models of the implosions and inform the design of DT-filled experiments to demonstrate ignition and propagating burn.

This paper is organized as follows. Section II presents a model for how the secondary yields change as a function of fuel-ρR and stopping power, and outlines how the combined information of the secondary yields is used to infer $\rho R_{fuel}, T_e$, and mix. The simplest form of the model assumes a plasma with uniform density and temperature, and is directly applicable to implosions containing deuterium fuel with dopants such as argon and krypton, or additional fuels such as ^{3}He or T. Section III presents the results of applying this model to experiments at the NIF. Finally, conclusions of the work are discussed in Section IV.

II. MODEL OF SECONDARY YIELDS

Secondary yield production depends on the path-averaged fusion reactivity of the D-D fusion products ^{3}He and T as they transit the plasma. Since fusion reactivity is a strong function of center-of-mass energy of the reactant particles, the stopping power of the plasma along the path of these products will have a strong impact on the secondary yields. An example calculation of a DD-^{3}He and DD-triton slowing in a homogenous, pure deuterium plasma, and the resulting cross-section for fusion with background deuterons, is shown in Figure 1. More generally, for a ^{3}He or T born at location $\vec{x}_0$ and following path $\vec{x}$, the probability P_2 of undergoing secondary fusion is:

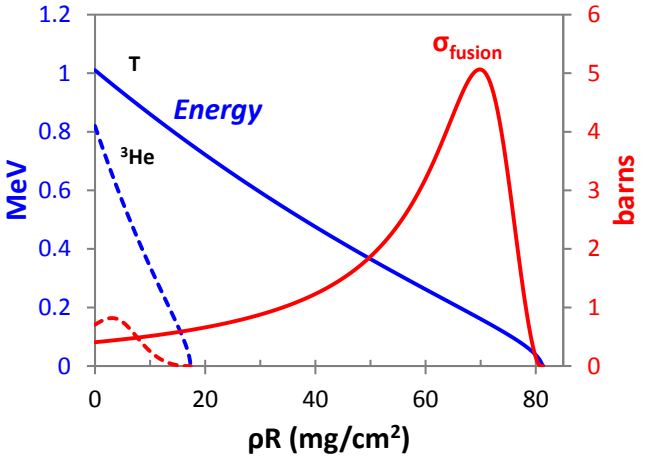

FIG. 1. Energy (blue, left axis) of a DD-triton (solid) and DD-^{3}He (dashed), and the resulting fusion cross section with the thermal deuterons (red, right axis), as a function of areal density traversed as they slow in a homogenous, pure deuterium plasma (ρ = 1 g/cc, $T_e = T_i$ =3 keV). The initially 0.8 MeV DD-^{3}He and 1.01 MeV DD-t lose energy to the plasma along their path, which is calculated using the Li-Petrasso model of plasma stopping power.[28, 29] If the areal density is sufficiently high the particles are ranged out in the plasma: in this example, the ^{3}He and T particles have ranges of ~18 and ~80 mg/cm^2, respectively. The cross-section is a strong function of the collisional center-of-mass energy, and therefore varies with the ρR transited as well. The ^{3}He ion is born near the peak in the D-^{3}He reactivity, so additional ρR tends to decrease the cross-section; in contrast, the triton is born with substantially more energy than the reactivity peak, and so the cross-section increases with higher ρR.

$$P_2 = \int_{\vec{x}} n_D(\vec{r})\,\sigma_{fusion}\left(\frac{2}{5}E(\vec{r})\right)d\vec{r}, \tag{3}$$

$$E(\vec{r}) = E_0 - \int_{\vec{x}_0}^{\vec{r}} \frac{dE}{dx}\left(E(\vec{x}'), T(\vec{x}'), n(\vec{x}')\right)d\vec{x}' \tag{4}$$

where n_D is the deuterium number density; $\sigma_{fusion}(E)$ is the cross-section for fusion of the ion with a deuteron, which is a function of the center-of-mass energy; $E(\vec{r})$ is the ion energy at point $\vec{r}$, and dE/dx is the plasma stopping power, which is a function of the ion energy and the local plasma properties. The factor of 2/5 is the ratio of the reduced mass to the reactant ion mass, and converts the ion kinetic energy to the center-of-mass energy. The probability of fusion for any one particle integrates over the plasma density and cross-section along its path. The cross-section in turn depends on the plasma

stopping power along the path, which is set by plasma temperature, density, and composition.

In the case of secondary fusion, the center-of-mass energy used in the calculation of the cross-section is dominated by the kinetic energy of the primary fusion product. The DD-^{3}He birth energy (0.82 MeV) puts this ion near the peak of the D^{3}He-fusion cross section (0.66 MeV). Because of this, increasing the plasma stopping power tends to reduce the average reactivity. In contrast, the DD-triton birth energy (1.01 MeV) is approximately six times more energetic than the peak of the DT-fusion cross section (0.16 MeV): the DT reactivity increases by as much as a factor of 12 as the triton slows in the fuel. These changes in the reactivity with slowing in the fuel are illustrated in Figure 1.

The measured ratio of secondary yield to primary yield, Y_2/Y_1, is a double-average of the probability in Equation 3: a primary-burn weighted average of the initial reactant location $\vec{x}_0$, and an average of the trajectory direction $\vec{x}$ over 4π of solid angle. This calculation is analytically intractable even for simple cases, but is accessible to numerical methods. A numerical model of secondary yield production was developed, using the Li-Petrasso stopping power formulation to range reactant products in a plasma,[28, 29] and the fusion cross-section parametrization of Bosch and Hale to calculate the probability of secondary fusion for both D^{3}He-protons and DT-neutrons.[13] This model, which calculates the probability of secondary production assuming a uniform plasma with a known density, temperature, and composition, is applied here to study the trends in secondary yield production.

As an illustrative case, the secondary yield production from a uniform, spherical deuterium plasma with various average areal densities $\langle \rho R_{deuterium} \rangle$ is shown in Figure 2.[30] The secondary yield production probability Y_2/Y_1 scales approximately linearly with average fuel-ρR, until the ^{3}He or T are stopped by the plasma, at which point the ratio saturates.[22] The range of the reactant ions, and therefore the saturation value of Y_2/Y_1, depends sensitively on the stopping power of the plasma. In weakly-coupled plasmas, the ions slow predominantly through collisions with the electrons, and the stopping power scales approximately as $T_e^{-3/2}$. An increased electron temperature therefore decreases the average stopping power, leading to increased ion ranges and increased probability of secondary fusion, as shown in Figure 2a). However changes in the plasma composition dilute the deuterium and can increase electron density, causing increased stopping power and reduced probability of secondary fusion, as shown in Figure 2b). An analytical scaling for this behavior is derived in Section II A Since the DD-^{3}He is ranged out at a lower ρR than the DD-t, the trends in secondary yield probability are divided into three regions: low-ρR, for which both the ^{3}He and T escape the plasma; medium-ρR, for which the ^{3}He is ranged out but the T escapes, and high-ρR, for which both products are ranged out. In the middle region,

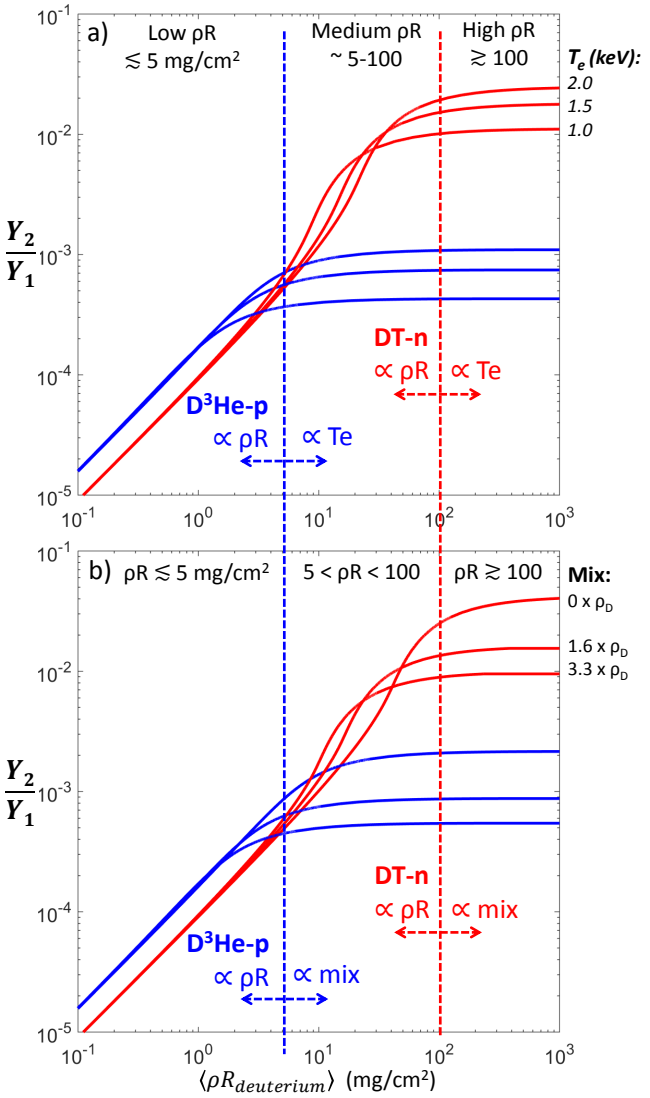

FIG. 2. Production probability for secondary D^{3}He-protons (blue) and DT-neutrons (red) as a function of ρR for various a) electron temperatures T_e and b) uniform CH mix. The example assumes a uniform deuterium plasma with $\rho =$ 0.21 g/cc, $T_i = 3.4$ keV (for the mix study, $T_e = T_i$). The range of the DD-^{3}He (blue dashed) and DD-t (red dashed) divide the plot into three regions: low ρR ($\lesssim$5 mg/cm^2), for which both secondary products are produced proportionally to ρR; medium ρR ($5 \lesssim \rho R \lesssim$100 mg/cm^2), for which the D^{3}He-proton yield saturates at a level governed by the stopping power (T_e or mix) and the DT-neutron yield continues to scale with ρR; and high ρR ($\gtrsim$100 mg/cm^2), for which both yields saturate and ρR cannot be inferred.

which occurs between approximately 5 and 100 mg/cm^2, measuring both secondary yields provides a strong constraint on both the ρR and the total stopping power in the plasma.

To highlight this behavior, Figure 3 shows the ratio of secondary neutron to secondary proton yields versus the deuterium areal density in the fuel ($\rho R_{deuterium}$) for

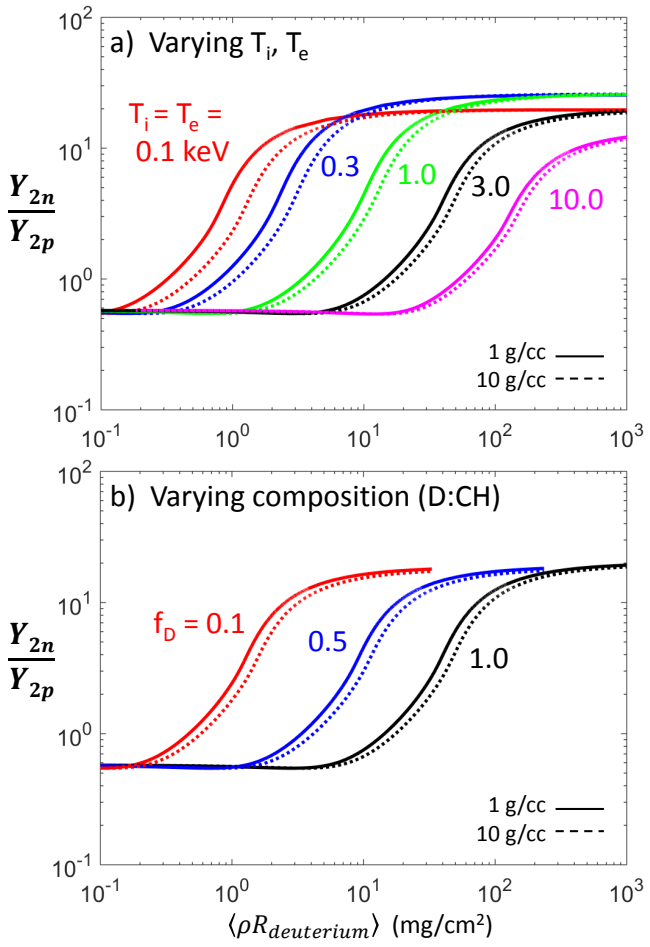

FIG. 3. The ratio of secondary DT-neutron yield to secondary D^{3}He-proton yield (Y_{2n}/Y_{2p}) as a function of the deuterium areal density in the fuel ($\rho R_{deuterium}$). The ratio is affected by the plasma stopping power, which varies with a) temperatures ($T_i = T_e$, from 0.1 to 10 keV in a pure deuterium plasma) and b) plasma composition (deuterium with plastic admixture: the deuterium fraction $f_D = n_D/(n_D + n_{CH})$ ranges from 0.1 to 1.0; $T_i = T_e = 3$ keV for this calculation). Curves are plotted for plasma density of 1 g/cc (solid) and 10 g/cc (dashed). Each curve varies rapidly for values of ρR in between the respective ranges of the DD-^{3}He and DD-t. The region of $\rho R_{deuterium}$ in which Y_{2n}/Y_{2p} changes rapidly depends on the plasma stopping power. Below and above the region of rapid change, the ratio of secondary neutrons to secondary protons is nearly constant.

a uniform plasma with a variety of temperatures and compositions.[31][32] Each curve is divided into three regions, defined by the respective ranges of a DD-^{3}He and DD-triton in that plasma. At low average fuel ρRs, both reactant ions escape the plasma, and the ratio of secondary yields varies slowly, with a value of approximately 0.6. As the ^{3}He is ranged below the peak of its fusion cross section, the ratio of secondary yields begins to rise rapidly. The curve plateaus at a value of approximately 20 when the triton is ranged out. The ranges of $\rho R_{deuterium}$ for which the curve varies rapidly is highly sensitive to the stopping power of the plasma, which depends on the plasma temperature and composition. This figure highlights the fact that by measuring both of the secondary yields, the ratio between them (Y_{2n}/Y_{2p}) contains information on the stopping power of the plasma, as long as the ρR is within a certain range. Since both mix and plasma electron temperature affect the stopping power, these two values are degenerate in terms of inferring a change in stopping power from the secondary yields. Additional information about the composition or electron temperature of the fuel is required to break this degeneracy.

The measured primary and secondary yields from experiments with moderate areal density can be interpreted in the following way. The ratio of secondary neutrons to primary neutrons is used to infer the areal density, as this ratio continues to grow roughly linearly with ρR in this regime. The (saturated) ratio of secondary protons to primary neutrons is primarily sensitive to the stopping power in this regime, and provides information on either the electron temperature or the plasma composition, depending on the experiment. In practice, a fully general analysis is used which simultaneously compares both ratios to the predicted ratios calculated for a range of ρR and either T_e or mix masses. A χ^2 method is then applied to determine the best fit between the experimental data and the model, and to infer the uncertainty in the evaluated quantities; the details of this method are presented in Appendix A. This approach is applied to data from three NIF campaigns in Section III. The analysis technique is applicable to any experiment where primary yields and both secondary yields are measured. It is worth noting that while both ρR and a quantity related to the stopping power may be accurately inferred only from implosions with moderate ρR, outside of this range useful information is still obtained. For low-ρR implosions in which neither the ^{3}He or T are ranged out, both secondary channels may be used to infer the ρR; whereas for high-ρR implosions in which both products are ranged out, both channels may be used to infer information about T_e or mix.

This method makes use only of the measured primary and secondary yields, and does not incorporate higher-order information contained in the secondary yield spectra. Spectral measurements have previously been used to compensate for stopping power effects when inferring ρR from secondary yields.[19, 20] In principle the spectral information could be used to break the degeneracy between T_e and mix, since the spectral shape is a function of ρR_{total} while the yield ratios are predominantly a function of $\rho R_{deuterium}$. In practice the low absolute yields of secondary DT-neutrons on many experiments considered here make precise spectral measurements difficult. D^{3}He-proton spectra are accurately measured at the relevant yields,[33] however the protons can lose a significant fraction of their energy via Coulomb collisions as they escape the experiment, which can distort the spectral shape. Incorporation of the spectral information into

this analysis is a valuable area of ongoing research.

Some differences exist between the Li-Petrasso model of plasma stopping power used here and other models of plasma stopping power in common use.[34] A second stopping power model based on Zimmerman's parametrization of the Maynard-Deutsch theory[35, 36] was also implemented to compare the simulated secondary yield production. In the low-ρR regime, secondary production was consistent using the two models, which is unsurprising because secondary yield production scales linearly with ρR in this regime. However secondary production did vary on the order of 10% between models in higher-ρR regimes when the reactant ion is ranged out. These modeling differences primarily affect the inference of T_e and mix, with only a small change in the inferred ρR. When applied to the data, the model differences were not larger than the measurement uncertainties, and therefore the results presented in Section III are not significantly affected by the choice of model. In the future, improved nuclear yield measurements and plasma characterization by other diagnostics may make secondary yield studies a viable approach for differentiating between plasma stopping power models.

A. The impact of plasma composition on secondary yield production

The effect of mix on the stopping power can be calculated numerically, as above; however, an analytical approach offers some insight into how the secondary yields scale with mix. Consider a uniform deuterium plasma with n uniformly mixed ion species, with charge state $Z_1^\star, \ldots, Z_n^\star$ and ion number fraction $f_1, \ldots, f_n$, with $f_k = n_k/n_{i,tot}$ such that $f_D + \sum_k^n f_k = 1$. The electron density in such a plasma will be $n_e = n_{i,tot}(f_D + \sum_k^n Z_k^\star f_k)$. Since the reactant ions slow down primarily on electrons in this regime, $dE/dx \propto n_e$.[28] Assuming the fuel areal density is high enough to stop the reactant ions, the probability of secondary fusion will then scale in the following manner:

$$P_2 = \int_{E_0}^{0} \frac{n_D \sigma_{fus}(E)}{dE/dx} dE = \frac{f_D}{f_D + \sum_k^n Z_k^\star f_k} P_2^0. \quad (5)$$

Here, the probability of secondary fusion from equation 3 has been recast as an integral over energy, and P_2^0 is the probability for secondary fusion in a pure deuterium plasma with the same deuterium density and temperature. Adding uniformly mixed ions into the plasma inhibits secondary yield production in two ways: by increasing the stopping power through increased electron density, and by diluting the deuterium ions. This scaling holds regardless of fuel density, so long as the reactant ions are stopped in the plasma and stopping is primarily on electrons.

Equation 5 can be generalized by fixing the final limiting energy of the reactant particle at a non-zero value E'. In this case, the dependence of the integral on the deuterium fraction may still be removed, leaving the relation:

$$P_2 \frac{f_D + \sum_k^n Z_k^\star f_k}{f_D} = F(E'), \quad (6)$$

where F is a function of E'.[37] If the charge-to-mass ratio ($Z^\star/A$) is equal to that for deuterium (1/2), the relationship between electron density and ρR_{total} is fixed and the final reactant particle energy is a function of ρR_{total} only. In this case, Equation 6 provides a simple relationship between the probability of secondary yield production in plasmas with equal ρR_{total} as the plasma composition is varied. In the limit of low ρR, F is then approximately equal to ρR_{total} multiplied by $0.1/(\mathrm{g/cm^2})$ for secondary DT-neutrons or $0.17/(\mathrm{g/cm^2})$ for secondary D^3He-protons.

The accuracy of Equation 6 was studied numerically for a wide variety of plasma conditions and over the entire range of areal density; an example calculation is shown in Figure 4. This secondary yield scaling appears to be accurate for both secondary products to within 10% in plasmas with D and ^4He with densities between 0.1–1 g/cc, temperatures between 0.1–10 keV, and deuterium fractions between 0.1–1. For deuterium-^3He mixtures in this range the agreement is within 20%. For deuterium-hydrogen mixtures in this range, the scaling is accurate to within 10% for temperatures between 0.1–1 keV, but only to within 30% at temperatures of 10 keV: this is most likely due to the increased importance of stopping on the hydrogen ions at high plasma temperatures. The full numerical modeling of the stopping power used in the remainder of this work intrinsically incorporates the details of plasma composition.

The uniform mix model presented here is most directly relevant to the case of ICF targets initially filled with deuterium and additional gases, such as low levels of dopants for x-ray imaging (Ar, Kr) or other fusion fuels (^3He, T). The DD implosion database for indirect drive at OMEGA includes several examples of implosions with 10 atm D_2 fuel doped with 0.05 atm Ar.[38] In such an implosion, assuming helium-like argon (Z = 16), the scaling in equation 5 predicts that the secondary yield will only be reduced by ∼4% compared to the pure-deuterium case. However, in targets with 50:50 mixtures of D^3He, which are routinely imploded on the OMEGA laser as backlighters for monoenergetic proton radiography experiments[39] and have been used in studies of kinetic plasma dynamics[27, 40, 41], the secondary yields are expected to be reduced by 67% compared to a pure-deuterium case. Diagnosis of the secondary D^3He-protons from D^3He-gas filled implosions is difficult due to a primary D^3He-proton yield several orders of magnitude larger, however the secondary DT-neutrons may in principle be measured. In symmetry (SymCap) and convergent-ablator (ConA) surrogate experiments at the NIF, for which D^3He fuel with deuterium fraction of 30% are imploded and reach average fuel areal densities ex-

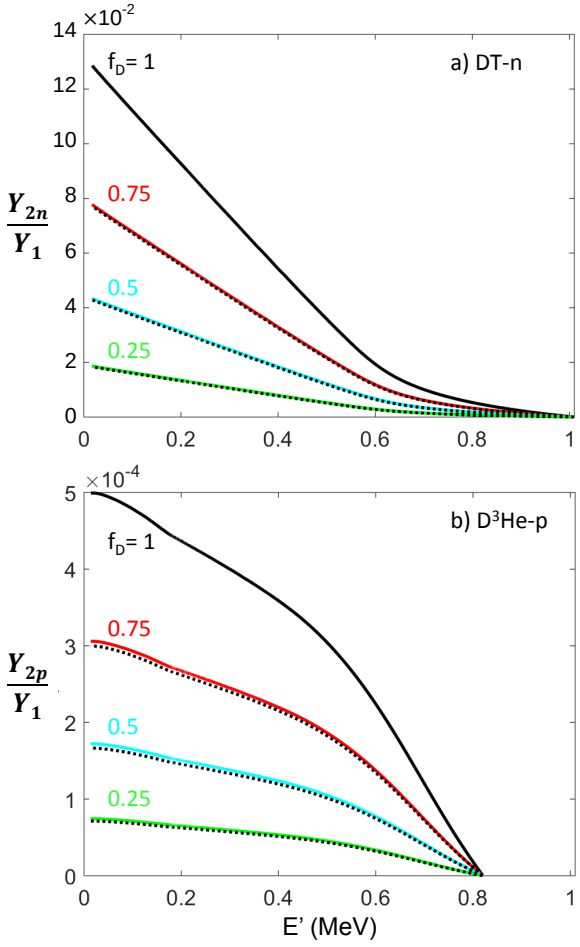

FIG. 4. Probability of secondary yield production for a) DT-neutrons and b) D^3He-protons as a function of the remaining energy E' of the escaping reactant particle (t or ^3He, respectively), for a D^3He plasma with $\rho = 1$ g/cc and $T_e = T_i = 1$ keV. Curves are calculated for deuterium fraction $f_D = 1$ (black), 0.75 (red), 0.5 (cyan) and 0.25 (green). When the $f_D = 1$ curve is multiplied with the scaling coefficient derived in Eqn. 6 (black dashed), the adjusted curves are in close agreement with the calculated lines.

ceeding 100 mg/cm^2, the above scaling indicates that the secondary yields will be reduced by 80% compared to a pure deuterium implosion.

This model can also be used to estimate the impact of non-uniform mix. Consider a pure deuterium core surrounded by a spherical shell region containing deuterium with uniform mix of a species with charge Z_m and number fraction f_m. The reactant particles initially transit the pure deuterium core, during which they are ranged down from the initial energy E_0 to E_1, and in the process produce $F(E1)$ secondary reactions. Next, they enter the mixed plasma, where they lose some additional energy $\Delta E > 0$ and produce $[F(E_1 - \Delta E) - F(E_1)][f_D/(f_D + Z_m f_m)]$ secondary reactions. The total secondary production is then given by:

$$P_{tot} = \frac{F(E_1)Z_m f_m + F(E_1 - \Delta E) f_D}{Z_m f_m + f_D} \quad (7)$$

Equation 7 indicates that the total production in this shell model is intermediate between the limiting case of pure deuterium fuel ($\Delta E \ll (E_0 - E_1)$) and the limit of uniform mix ($\Delta E \gg (E_0 - E_1)$). By assuming a uniform model, a smaller mix fraction is inferred than is actually present in the mixed regions. After accounting for the volume of the shell, the total mixed mass is also underestimated by assuming uniform mix. Accounting for profiles of mix in the future will improve the accuracy and range of application for this technique.

III. ANALYSIS OF EXPERIMENTAL DATA FROM THE NIF

The combined secondary yield analysis was applied to data recorded on several experiments performed at the National Ignition Facility. The indirect-drive ignition relevant experiments produce fuel assemblies with very high areal density on the order of hundreds of mg/cm^2, and the secondary protons are partially or fully ranged out in the implosion. As such this technique cannot be applied to them. However several experimental campaigns have investigated plasmas with moderate areal density and pure deuterium fuel. This section will present the secondary yield data and combined secondary yield analysis for three campaigns: polar-direct-drive exploding pushers, indirect-drive 1-shock and 2-shock implosions, and the polar-direct-drive defect-induced mix experiments (DIME). A summary of all target and laser parameters as well as measured yields and burn-averaged ion temperatures for these experiments is provided in Table I.

The analysis technique is contingent upon robust measurements of both the D^3He-proton and the DT-neutron spectra in deuterium-filled implosions. Proton spectra are routinely recorded at the NIF using the Wedge Range Filter (WRF) spectrometers,[9, 33, 42] while secondary neutron yields are recorded by neutron Time-of-Flight (nTOF) detectors.[43, 44] Time-of-flight is used to resolve neutron energy and differentiate secondary neutrons from the primary 2.45 MeV neutrons, which are 10^2 to 10^4 times more plentiful.

A. Polar-direct-drive exploding pushers

Shock-driven 'exploding pusher' implosions are used on the NIF primarily for diagnostic calibration, although careful analysis of the experimental data has provided insights into kinetic processes in the shock-convergence phase of ICF.[45] Because these implosions are gas-filled (ρ_0=1.6 mg/cc) and have low convergence (CR∼5), the fuel ρR at bang-time is expected to be low. Specifically,

TABLE I. Target and laser parameters and measured DD-burn averaged ion temperatures and yields for the NIF experiments used in the combined secondary yield study: exploding pushers (ExpPush, see Section III A), indirect-drive exploding pushers (IDEP, see Section III B), and defect-induced mix experiments (DIME, see Section III C). All capsules were filled with pure D_2 gas.

Campaign	Shot	OD μm	wall μm	fill mg/cc	Energy kJ	Pulse ns	$\langle T_i \rangle_{DD}$ keV	Y_{DD}	$Y2_{D^3He}$	$Y2_{DT}$
ExpPush	N110131	1555	4.5 SiO_2	1.6	52	2.1	5.4 ± 0.2	$3.0 \pm 0.1 \times 10^{11}$	$2.0 \pm 0.4 \times 10^{8}$	$8.6 \pm 1.0 \times 10^{7}$
	N130129	1533	4.6 SiO_2	1.6	51.4	1.4	3.9 ± 0.3	$2.5 \pm 0.2 \times 10^{11}$	$1.7 \pm 0.3 \times 10^{8}$	$7.6 \pm 2.8 \times 10^{7}$
IDEP	N130312	2110	120 CH	6.3	892	1-shock	3.5 ± 0.2	$5.2 \pm 0.2 \times 10^{12}$	$6.6 \pm 0.9 \times 10^{9}$	$0.96 \pm 0.08 \times 10^{10}$
	N130813	2167	83.5 HDC	3.0	1290	2-shock	3.6 ± 0.2	$22 \pm 2 \times 10^{12}$	$14 \pm 7 \times 10^{9}$	$13.5 \pm 1.3 \times 10^{10}$
DIME	N120728	2200	40 CH	0.82	666	2.1	4.4 ± 0.3	$5.8 \pm 0.4 \times 10^{11}$	$2.1 \pm 0.4 \times 10^{8}$	$2.8 \pm 0.3 \times 10^{8}$
	N120730	2200	40 CH†	0.82	665	2.1	4.2 ± 0.3	$6.5 \pm 0.4 \times 10^{11}$	$2.2 \pm 0.4 \times 10^{8}$	$3.5 \pm 0.3 \times 10^{8}$
	N121119	2200	40 CH	0.82	659	2.1	4.3 ± 0.4	$8.6 \pm 0.4 \times 10^{11}$	$3.7 \pm 0.7 \times 10^{8}$	$6.2 \pm 0.6 \times 10^{8}$
	N121207	2200	42 CH	0.82	607	2.1	3.4 ± 0.2	$3.7 \pm 0.2 \times 10^{11}$	$1.9 \pm 0.4 \times 10^{8}$	$2.4 \pm 0.2 \times 10^{8}$
	N130320	2200	42 CH	0.82	319	2.1	3.7 ± 0.2	$7.3 \pm 0.2 \times 10^{11}$	$5.8 \pm 1.2 \times 10^{8}$	$10.3 \pm 1.0 \times 10^{8}$
	N130321	2200	42 CH	0.82	463	2.1	3.8 ± 0.2	$6.0 \pm 0.2 \times 10^{11}$	$4.0 \pm 0.8 \times 10^{8}$	$5.1 \pm 0.5 \times 10^{8}$

† Capsule fabricated with an equatorial groove to induce mix

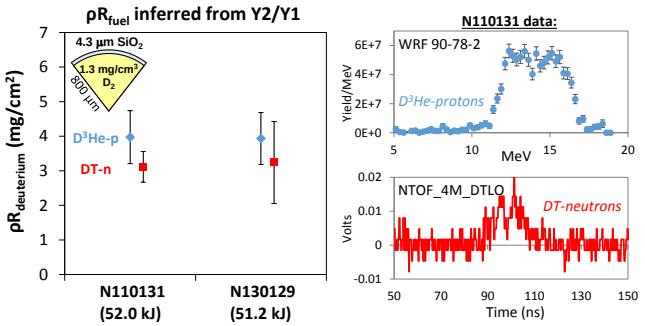

FIG. 5. (left) Fuel ρR was inferred from both secondary D^3He-p (blue) and DT-n (red) yields on two NIF polar-direct drive (PDD) Exploding Pushers, N110131 and N130129. Target details are inset. Primary nuclear production was assumed to occur uniformly throughout the fuel. For both shots, the ρR inferred from each secondary product was in agreement. These experiments have a low fuel ρR such that the DD-^{3}He are not ranged out and only ρR can be robustly inferred. (right) Raw D^3He-proton spectrum (top) and DT-neutron time-history (bottom) recorded on shot N110131.

the initial fuel areal density $\rho R_0 \approx 0.13$ mg/cm^2 is expected to grow by a factor of $(\mathrm{CR})^2 \sim 25$, so a final value of < 5 mg/cm^2 is expected.[46] This expectation is confirmed by the data from two implosions, shown in Figure 5. The fuel ρR inferred separately from both secondary products were found to agree with each other, with a value of ~ 3–4 mg/cm^2.

These experiments are in the 'low' ρR region of Figure 2, and as such the yield of both secondary products is expected to scale linearly with ρR, and neither T_e nor mix can be robustly inferred. However, the data can be used to infer an upper bound on the amount of fuel-shell mix present in the experiments. Introducing mix of silicon and oxygen ions from the glass shells increases the total areal density in the fuel without increasing the deuterium areal density. Therefore sufficient mix would range out the DD-^{3}He sooner than expected, and increase the secondary neutron-to-proton ratio. An electron temperature equal to 0.67 and 0.75 times the measured burn-averaged ion temperature was assumed for N110131 and N130129, respectively, based on the results of 1D-LILAC simulations of these implosions.[45, 47] Under this assumption, the amount of mix required for inconsistency with the measured secondary yield data was determined to be 6.0 μg for N110131 and 3.6 μg for N130129. Figure 6 shows a map of χ^2 as a function of mix mass and ρR for both shots, as well as the simulated secondary generation curves for both the no-mix case and the upper-bound mix for each shot. Both sets of data are consistent with a clean implosion. The upper limit on mixed mass can be understood as the amount of areal density in addition to the deuterium areal density, which is inferred from $Y2/Y1$, that is necessary to range out DD-^{3}He ions. The slightly higher ρR_d and the slightly lower temperature inferred for N130129 translate into a higher average stopping power in the clean fuel that is closer to the range of the ^{3}He ions. Thus, the data from this shot allow less additional $rhoR$ in the fuel from mix than the data from N110131, and a reduced upper bound on the mix mass is inferred.

The upper bounds inferred here for mixed mass are quite large relative to realistic values, and would likely have a substantial impact on the implosion if true. For N130129, the greatest mixed mass that is consistent with the data would imply a plasma with an average ion charge of $\langle Z \rangle \approx 2.0$. Since radiative loss from bremsstrahlung emission scales proportionally to $\langle Z \rangle^2$, the upper-bound mix case would suffer from four times the radiative loss of a clean implosion, which might be expected to affect other experimental results such as nuclear yield or burn-average temperature. These quantities are matched well by simulations of this implosion,[48] suggesting that the mixed mass in the experiment is substantially less than the upper bound inferred here. This example underscores the need for a sufficiently high ρR in order to infer precise information about the fuel-averaged stopping power in

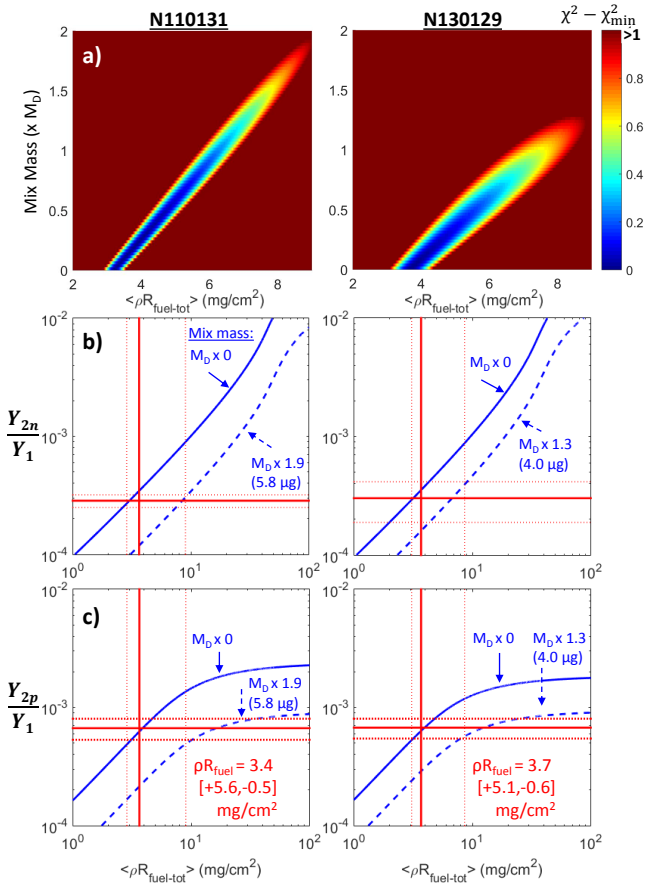

FIG. 6. Upper bound calculation for mix mass in two NIF Exploding Pusher implosions: N110131 (left) and N130129 (right). a) The values of fuel areal density and mix mass (as a fraction of the total deuterium mass M_D = 3.0 and 3.2 µg, respectively) for which $\chi^2 - \chi^2_{min} \leq 1$ are consistent with the observed secondary yield production. The simulated secondary-to-primary yield ratio as a function of fuel ρR are shown for b) neutrons and c) protons, for both a clean fuel and including the upper bound on mix mass. Measured secondary yield ratios with uncertainties (red horizontal lines), and inferred ρR with uncertainties (red vertical lines) are also shown.

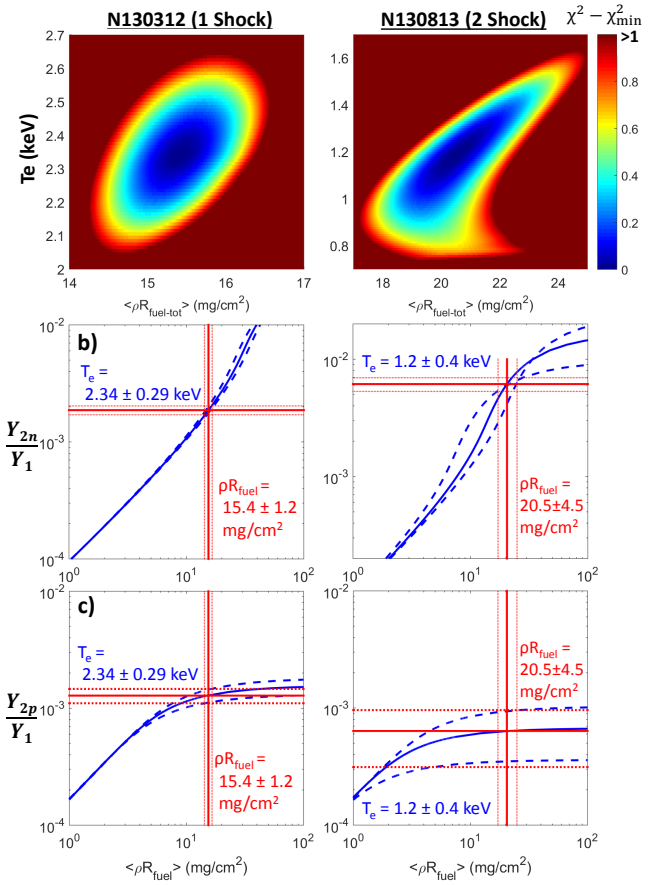

FIG. 7. Combined secondary yield analysis for the Indirect Drive implosions: N130312 1-shock (left) and N130813 2-shock (right). The analyses assume pure deuterium plasmas with ρ = 1.4 ± 0.43 mg/cc, T_i = 3.53 ± 0.18 keV for the 1-shock and ρ = 2.96 ± 0.89 mg/cc, T_i = 3.6 ± 0.2 keV for the 2-shock. a) The map of χ^2 showing regions of T_e and ρR_{fuel} that are consistent with the data. $\chi^2 - \chi^2_{min} > 1$ (red) indicates inconsistency. The calculated secondary yield production ratio for b) DT-neutrons and c) D^{3}He-protons is shown for the best-fit T_e with uncertainties (blue), along with the measured data and uncertainty (red horizontal lines) and inferred average ρR_{fuel} and uncertainty (red vertical lines).

the experiment.

B. Indirect-drive 1- and 2-shock implosions

The 'indirect drive exploding pusher' (IDEP) is a 1-shock implosion in which the ablator completely burns through, which was designed to provide a simple 1D-hydrodynamic implosion for verification of hydrodynamic codes. A D_2-filled and a DT-filled implosion using this platform each demonstrated optimally 1D performance and agreement across the board with simulated predictions.[49] Both secondary D^{3}He-protons and DT-neutrons were measured on the DD-filled implosion N130312, and the combined secondary yield analysis was performed as shown on the left in Figure 7. In this implosion, the average ρR_{fuel} was sufficiently high to range out the DD-^{3}He. Since the implosion demonstrated extraordinary agreement with the 1D simulations, hydrodynamic mix is considered to be negligible. As such, the data was used to determine the average ρR_{fuel} = 15.4 ± 1.2 mg/cm^2 and the average fuel electron temperature T_e = 2.35 ± 0.25 keV.

The inferred electron temperature is approximately 66% of the measured DD-neutron burn-averaged ion temperature ($\langle T_i \rangle$ = 3.53 ± 0.18 keV). This result most likely reflects a difference in the fuel-region weighting of each measurement: because of the strong reactivity scaling with ion temperature, the burn-averaged ion temperature is weighted toward the hotter regions of the

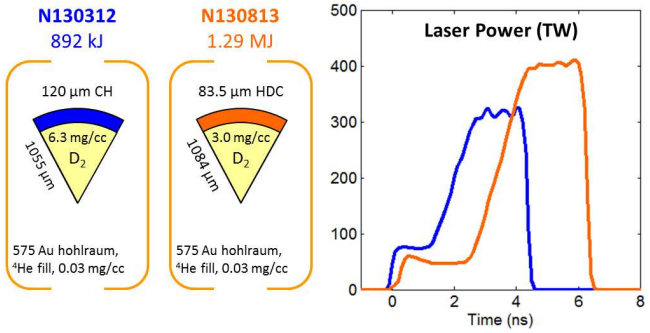

FIG. 8. Comparison of the targets and laser impulses for the 1-shock (indirect-drive exploding pusher) and 2-shock implosions on NIF: N130312 (blue) and N130813 (orange), respectively. In addition to increased laser energy for N130813, a major difference between the two implosions is the choice of shell material (CH and HDC, respectively).

plasma. In contrast, the electron temperature measured by the secondary yield analysis is averaged over the entire deuterium-containing volume, weighted to the nuclear burn history. Since the shock initially heats the ions, an alternative explanation for a smaller electron temperature would be that the electrons and ions are not fully equilibrated. Using the burn-averaged ion temperature and the inferred electron temperature and fuel density at burn, the electron-ion equilibration time was calculated to be $\tau_{ei} = \nu_{ei}^{-1} = 125$ ps.[50] This value is shorter than the implosion timescale but is comparable to the expected duration of nuclear production, and so insufficient equilibration may contribute to the low inferred ratio of T_e/T_i. The electrons will also cool more rapidly than the ions due to radiative emission and electron thermal conduction out of the hotspot, which will tend to reduce the electron temperature relative to the ion temperature in the fuel.

A 2-shock implosion was designed and performed to achieve higher density and convergence while maintaining 1D-hydrodynamic behavior of the fuel.[51] In this experiment, the ablator does not burn through and a deceleration phase compresses the fuel after the shock rebounds, as in the ignition design, but the fuel adiabat is higher than in ignition-relevant experiments and the implosion is less susceptible to hydrodynamic fuel-shell mix. This implosion used a high-density carbon target. A comparison of the targets and laser impulses for the 1-shock and 2-shock implosions is shown in Figure 8. The experiment was well-modeled using 1D-hydrodynamic simulations implying that fuel-shell mix was again negligible.

Both secondary products were observed on the 2-shock deuterium-filled implosion N130813, and the combined secondary yield analysis was performed to infer $\rho R = 20.5 \pm 4.5$ mg/cm^2 and $T_e = 1.2 \pm 0.4$ keV, as shown on the right in Figure 7. The fuel ρR was larger in the 2-shock implosion, as expected based on a higher observed convergence ratio (CR $\approx$ 11, as compared to $\approx$ 5 for the 1-shock implosion). The inferred electron temperature is colder in the 2-shock implosion by almost a factor of two, although the burn-averaged ion temperatures are comparable. Because of the increased density, the calculated electron-ion equilibration time for this experiment ($\tau_{ei} = 100$ ps) was slightly shorter than for the 1-shock experiment, indicating that the reduced temperature is not due to a change in the thermal coupling of the electron and ion fluids. Since the x-ray drive of the implosion is absorbed by electrons in the ablation front, the burn through of the ablator in the 1-shock implosion allows for direct heating of the core electrons by the x-ray drive, a mechanism that is not available in the 2-shock implosion. The 2-shock implosion is also designed to set the fuel on a lower adiabat than the 1-shock implosion, which is consistent with a lower observed fuel-averaged temperature.

Mix of carbon from the shell into the fuel could alternatively account for the low observed secondary proton yield, however a substantial amount (14 μg, greater than the initial deuterium fuel mass) would be necessary to allow the same T_e/T_i ratio observed on the 1-shock implosion. Given the agreement of 1D-hydrodynamic simulations with the observed data on this shot,[51] substantial mixed mass seems unlikely, supporting the electron temperature inference.

Notably, this data is approaching the regime where both the DD-^{3}He and DD-t are ranged out. Unlike for the 1-shock implosion, the calculated secondary neutron production models shown in Fig. 7b) are sensitive to both ρR and T_e in this regime. This data underscores the importance of the simultaneous χ^2 analysis, as the region in (ρR,T_e)-space that produces good fits (see Fig. 7a) develops a more complex shape. If the secondary proton yield was approximately 40% of the observed value, the data would be consistent with ranging out of the DD-tritons and an accurate ρR could not be inferred.

C. Defect-induced mix experiments (DIME)

A series of six deuterium-filled, polar-direct-drive experiments[52] was performed at the NIF in 2012 and 2013, as part of the defect induced mix experiments (DIME) campaign.[53] These experiments imploded 2.2 mm diameter CH capsules with a shell thickness of 40–42 μm and filled with 0.82 mg/cc D_2. The targets were illuminated using a flat-top laser drive with full-width at half maximum of 2.1 ns, containing between 319 and 666 kJ of laser energy. Observed primary DD-neutron yields were in the range 3–9$\times 10^{11}$, and secondary proton and neutron yields were recorded on all shots.

Since the electron temperature is unknown, both mix and electron temperature may be expected to modify the plasma stopping power. The inferred burn-averaged ion temperatures provide an upper limit on the volume-averaged plasma electron temperature during burn. Setting $T_e = \langle T_i \rangle$ in the analysis resulted in the ρR_{fuel} and mix masses shown in Figure 9. The amount of CH mixed

mass inferred in the experiments ranges from 8 to 29 μg, and increases monotonically with the laser drive energy. Because of the degeneracy in stopping power between colder T_e and increased mix, these mix masses can be taken as an upper bound. The inferred upper bound on the mixed masses correspond to a maximum of the innermost ∼2 μm of the shell mixing completely into the fuel. Each of these implosions had an initial total deuterium mass of 4.1 μg. Given the average mass of the mixed CH ions is 3.25× the deuteron mass, the number density of mixed ions inferred for the implosions ranges from 0.6–2.2× the number density of deuterium.

Although Figure 9 presents three quantities, only two independent quantities are inferred from the data. Mixed mass and total deuterium areal density in the fuel (b and c) are the most well-constrained quantities by the secondary data, while the total areal density in the fuel (a) is degenerate with the other two. As previously discussed, the secondary neutron analysis effectively constrains the deuterium ρR, while the secondary proton analysis effectively constrains the stopping power (in this case, mix).

In the indirect-drive 1-shock (IDEP) and 2-shock implosions, the electron temperature was significantly lower than the burn-averaged ion temperature, and this effect must be considered in the DIME implosions as well. To assess the dependence of the inferred mix on the electron temperature, the mix was evaluated for various T_e in one of the implosions (N130320). The resulting trends, which are shown in Figure 10, show an approximately linear relationship between increased T_e and increased inferred mix. The inferred $\langle T_i \rangle$ is shown for reference. This experiment is the most similar to a subsequent implosion of an H_2-filled CD-shell (N130618) in which neutron diagnostics were used to constrain the mixed mass, which is also shown on the figure along with a simulated value.[54] The secondary-inferred mix is consistent with the mix measurement from N130618 for electron temperatures in the range $\sim 3.3 \pm 0.7$ keV, which is in rough agreement with the observed burn-averaged ion temperature. It is worth noting, however, that this technique can in principle diagnose the presence of cold mix mass in the fuel, which would not be visible using x-ray techniques. This data illustrates that use of the secondary yields to robustly measure a mixed mass in the fuel requires additional knowledge of the electron temperature in the fuel. Methods for measuring the fuel electron temperature, such as comparing the relative x-ray self-emission signal observed through several filter materials, have been developed at the NIF and will reinforce the value of the combined secondary product data.[55]

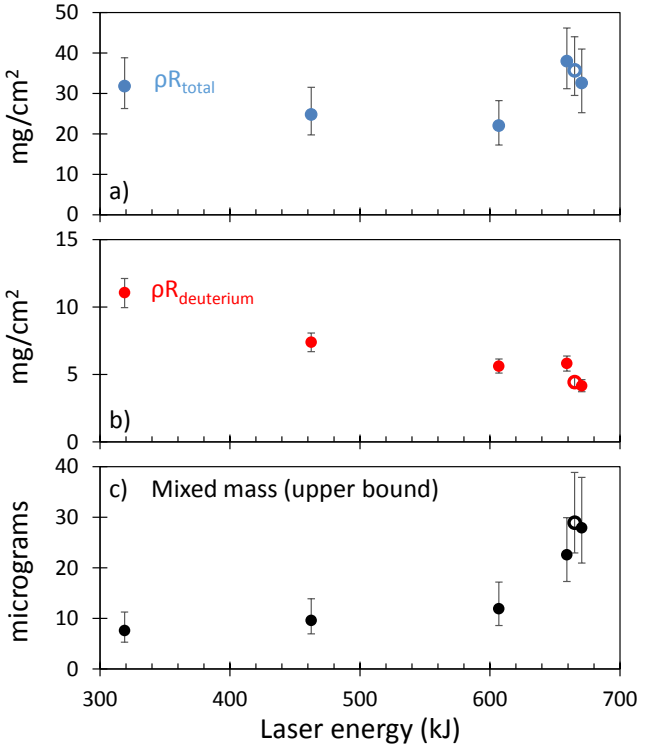

FIG. 9. Inferred values from secondary yield data recorded on the defect induced-mix experiments (DIME) performed on the NIF, plotted as a function of laser energy: a) the average total ρR in the fuel region (blue) and b) the average deuterium ρR in the fuel region (red); c) the mixed mass inferred in the fuel region (black). Increased laser energy is associated with increased mix. T_e, which is degenerate with mix for this analysis, was set equal to the measured burn-averaged ion temperature in this calculation; therefore the mixed mass should be taken as an upper bound. The target with a machined equatorial defect (N120730, hollow point) shows no measurable difference from the spherical targets.

IV. CONCLUSION

A technique has been developed to infer the average fuel areal density during burn, and either the average fuel electron temperature or the average mix mass in the fuel during burn, using the combined information from the secondary DT-neutron and D^3He-proton yields from deuterium-filled implosions. The reactivity for the secondary D^3He (DT) reaction decreases (increases) as the ^3He (t) ion slows in the plasma. Because of this difference, and because the range of the triton is an order of magnitude larger than that of the ^3He ion, the ratio of the secondary proton to secondary neutron yields changes with both the average deuterium ρR and with the average stopping power of the plasma. By invoking a model of the stopping power, the combined primary and secondary yield information is used to infer the areal density as well as the T_e or the mix mass for implosions with moderate fuel ρR in the range $\sim$ 5–100 mg/cm^2. This technique has been applied to three classes of NIF implosions: polar-direct-drive exploding pushers with low ρR; indirect-drive 1-shock (IDEP) and 2-shock implosions, for which mix was negligible and $T_e = 0.33 - -0.67\langle T_i \rangle$ was inferred; and the polar-direct-drive DIME campaign, for which significant mix was observed.

The model developed here is essentially zero-

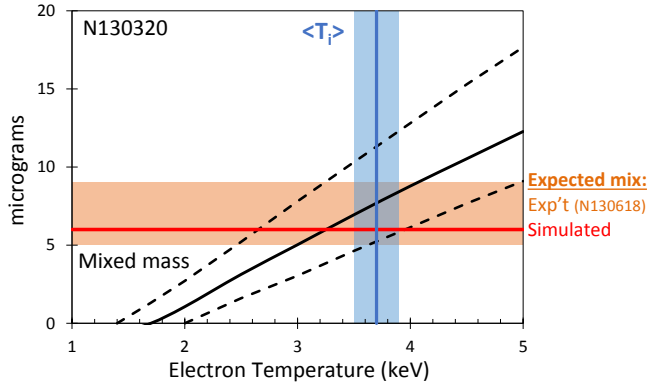

FIG. 10. Variation of the inferred mix mass with the value assumed for T_e in the analysis of the secondary yields from the DIME implosion N130320. The inferred mix mass (black) and uncertainty (black dashed) increase approximately linearly with the assumed plasma electron temperature, because both T_e and mix affect the plasma stopping power. The mix values inferred from neutronics measurements on a comparable shot N130618[54] (orange) and from simulations (red) are in agreement with the secondary-inferred mix values for $T_e \approx 3.3 \pm 0.7$ keV. This value is consistent with the measured burn-averaged ion temperature $\langle T_i \rangle = 3.7 \pm 0.2$ keV (blue).

dimensional, assuming a uniform plasma during burn. Temperature and density profiles vary with radius in 1D-simulations, which would have an effect on reactant slowing in the plasma and secondary production. Mixed mass will also vary with radius, being generally largest near its source at the fuel-shell interface. More precise comparisons with experiments will require incorporation of more realistic spatial models. Previous research has implemented Monte Carlo simulation for secondary yields based on 1D profiles,[23] which could be done for this analysis as well. Fundamentally, three pieces of information are being used in this approach – the primary and secondary yields – and therefore at most three pieces of information can be inferred, which is not sufficient to constrain profiles of density, temperature, and mix. The accuracy of this technique can be extended through analysis of the spectral information from the secondary products, as well as the incorporation of additional experimental data about the fuel such as electron temperature profiles measured using x-ray diagnostics. The ultimate application of this analysis is in support of a larger diagnostic effort to understand as well as possible the state of the fusing plasma. In particular this technique will provide valuable insight for the development of polar direct-drive experiments as one path towards attaining ignition on the NIF.

The authors thank the engineering and operations staff at NIF, LLE, and MIT for their support. This work was performed under the auspices of the U.S. Department of Energy by Lawrence Livermore National Laboratory under Contract DE-AC52-07NA27344. This work was done in part for H. Rinderknecht's Ph.D. thesis and was supported in part by the U.S. DoE (DE-FG52-09NA29553), LLNL (B580243), LLE (414090-G), the Fusion Science Center at the University of Rochester (415023-G), and the National Laser Users Facility (DE-NA0000877).

Appendix A: Reduced χ^2 inference method

The analysis method used in this work utilizes a reduced-χ^2 approach to find the best fit of the secondary production models to the experimental data and analyze the uncertainty in the inferred parameters. A basic description of the χ^2 method is presented here for clarity, although χ^2 methods are widely used; see Ref. [56] for a more general overview. Given a model P which takes as input M parameters p_j that is expected to predict a data set with N points x_k (N≤M), each of which has an uncertainty σ_k, the 'goodness' of a fit between the model and the data is defined as:

$$\chi^2 = \sum_k^N \frac{[x_k - P(p_1, ..., p_M)]^2}{\sigma_k^2} \tag{A1}$$

Since each measurement can be expected to be on average σ from the modeled value even for an accurate model, a minimum value $\chi^2_{min} = (N - M)$ is taken to describe a good fit, whereas all models with $\chi^2 - \chi^2_{min} \leq 1$ are within a 1-σ measurement uncertainty.

Three yield quantities are measured – the primary DD-neutron yield, the secondary DT-neutron yield and the secondary D^3He-proton yield. However the model predicts only the ratio of secondary to primary yields, and so only two effective data points are used. The uncertainties of the yield measurements are uncorrelated, so the uncertainty of the ratio is taken to be the reduced mean square sum of the primary and secondary yield measurement uncertainties.

The model parameters include density, areal density, electron temperature, ion temperature, and plasma composition of the fuel at burn. The full secondary production model is underconstrained by the data; however several of these parameters may be inferred from experimental data, initial conditions, and/or simulations with varying degrees of certainty. In this work, the plasma ion temperature has been set equal to the primary-burn averaged ion temperature as measured from the DD-neutron spectra,[57] and the density is inferred from the initial fuel density and x-ray measurements of convergence. As the stopping power is not strongly dependent on these parameters in the regimes of interest, these inferences are sufficient. This leaves three parameters – ρR, T_e, and mix – to be constrained by two observables. To perform this operation, either the plasma must be in a regime where it is insensitive to one of these parameters (i.e. low ρR, for which the yield ratios are insensitive to T_e and mix; or high ρR, for which the yield ratios are insensitive to ρR), or an additional assumption must be

made. Thus in Section III B, mix was expected to be negligible and T_e was inferred; whereas in Section III C, both mix and T_e effects are likely and additional information is required. Note that in principle when fitting two parameters to two datapoints, a perfect fit ($\chi^2 = 0$) for some set of parameters is expected as long as the model is sufficiently general. The uncertianties of the inputs then directly translate into uncertainties in the outputs, and the validity of the model cannot be tested unless additional data or constraints on the model are obtained.

After the problem is reduced to two free parameters (p_1, p_2), a range of likely values is determined for each parameter and the χ^2 is calculated for each pair of parameters on a dense grid. This step is repeated varying the grid range and density until a well-resolved population of acceptable answers is found, as shown in Fig. 6a) and 7a). The parameter value producing the minimum χ^2 are taken to be the best fit to the data, and the extrema of each parameter for which $\chi^2 \leq \chi^2_{min} + 1$ are taken as defining the 1-σ uncertainty range.

[1] J. Lindl, Physics of Plasmas **2**, 3933 (1995).
[2] C. D. Zhou and R. Betti, Physics of Plasmas **15**, 102707 (2008).
[3] O. N. Krokhin and V. B. Rozanov, Soviet Journal of Quantum Electronics **2**, 393 (1973).
[4] W. H. Goldstein, "Science of Fusion Ignition on NIF," Tech. Rep. LLNL-TR-570412 (Lawrence Livermore National Laboratory, 2012).
[5] D. Ress, R. A. Lerche, R. J. Ellis, S. M. Lane, and K. A. Nugent, Science **241**, 956 (1988).
[6] C. L. Ruiz, R. J. Leeper, F. A. Schmidlapp, G. Cooper, and D. J. Malbrough, Review of Scientific Instruments **63**, 4889 (1992).
[7] R. A. Lerche, D. W. Phillion, and G. L. Tietbohl, Review of Scientific Instruments **66**, 933 (1995).
[8] T. J. Murphy, C. W. Barnes, R. R. Berggren, P. Bradley, S. E. Caldwell, R. E. Chrien, J. R. Faulkner, P. L. Gobby, N. Hoffman, J. L. Jimerson, K. A. Klare, C. L. Lee, J. M. Mack, G. L. Morgan, J. A. Oertel, F. J. Swenson, P. J. Walsh, R. B. Walton, R. G. Watt, M. D. Wilke, D. C. Wilson, C. S. Young, S. W. Haan, R. A. Lerche, M. J. Moran, T. W. Phillips, T. C. Sangster, R. J. Leeper, C. L. Ruiz, G. W. Cooper, L. Disdier, A. Rouyer, A. Fedotoff, V. Y. Glebov, D. D. Meyerhofer, J. M. Soures, C. Stckl, J. A. Frenje, D. G. Hicks, C. K. Li, R. D. Petrasso, F. H. Seguin, K. Fletcher, S. Padalino, and R. K. Fisher, Review of Scientific Instruments **72** (2001).
[9] F. H. Séguin, J. A. Frenje, C. K. Li, D. G. Hicks, S. Kurebayashi, J. R. Rygg, B. E. Schwartz, R. D. Petrasso, S. Roberts, J. M. Soures, D. D. Meyerhofer, T. C. Sangster, J. P. Knauer, C. Sorce, V. Y. Glebov, C. Stoeckl, T. W. Phillips, R. J. Leeper, K. Fletcher, and S. Padalino, Review of Scientific Instruments **74**, 975 (2003).
[10] F. H. Séguin, J. L. DeCiantis, J. A. Frenje, S. Kurebayashi, C. K. Li, J. R. Rygg, C. Chen, V. Berube, B. E. Schwartz, R. D. Petrasso, V. A. Smalyuk, F. J. Marshall, J. P. Knauer, J. A. Delettrez, P. W. McKenty, D. D. Meyerhofer, S. Roberts, T. C. Sangster, K. Mikaelian, and H. S. Park, Review of Scientific Instruments **75**, 3520 (2004).
[11] J. R. Rygg, F. H. Séguin, C. K. Li, J. A. Frenje, M. J.-E. Manuel, R. D. Petrasso, R. Betti, J. A. Delettrez, O. V. Gotchev, J. P. Knauer, D. D. Meyerhofer, F. J. Marshall, C. Stoeckl, and W. Theobald, Science **319**, 1223 (2008).
[12] D. T. Casey, J. A. Frenje, M. Gatu Johnson, F. H. Séguin, C. K. Li, R. D. Petrasso, V. Y. Glebov, J. Katz, J. Magoon, D. D. Meyerhofer, T. C. Sangster, M. Shoup, J. Ulreich, R. C. Ashabranner, R. M. Bionta, A. C. Carpenter, B. Felker, H. Y. Khater, S. LePape, A. MacKinnon, M. A. McKernan, M. Moran, J. R. Rygg, M. F. Yeoman, R. Zacharias, R. J. Leeper, K. Fletcher, M. Farrell, D. Jasion, J. Kilkenny, and R. Paguio, Review of Scientific Instruments **84**, 043506 (2013).
[13] H.-S. Bosch and G. M. Hale, Nuclear Fusion **32**, 611 (1992).
[14] H. D. Campbell and S. F. H., "Proceedings of the first topical meeting on the technology of controlled nuclear fusion," (American Nuclear Society, LaGrange Park, IL, 1974) p. 75.
[15] E. G. Gamalii, S. Y. Gus'kov, O. N. Krokhin, and V. B. Rozanov, JETP Letters **21**, 70 (1975).
[16] S. Skupsky and S. Kacenjar, Journal of Applied Physics **52**, 2608 (1981), 10.1063/1.329070.
[17] T. E. Blue and D. B. Harris, Nucl. Sci. Eng. **77**, 463 (1981).
[18] T. E. Blue, J. W. Blue, J. S. Durham, D. B. Harris, A. S. Hnesh, and J. J. Reyes, Journal of Applied Physics **54**, 615 (1983), 10.1063/1.332066.
[19] H. Azechi, N. Miyanaga, R. O. Stapf, K. Itoga, H. Nakaishi, M. Yamanaka, H. Shiraga, R. Tsuji, S. Ido, K. Nishihara, Y. Izawa, T. Yamanaka, and C. Yamanaka, Applied Physics Letters **49**, 555 (1986), 10.1063/1.97093.
[20] M. D. Cable and S. P. Hatchett, Journal of Applied Physics **62** (1987).
[21] H. Azechi, M. D. Cable, and R. O. Stapf, Laser and Particle Beams **9**, 119 (1991).
[22] F. H. Séguin, C. K. Li, J. A. Frenje, D. G. Hicks, K. M. Green, S. Kurebayashi, R. D. Petrasso, J. M. Soures, D. D. Meyerhofer, V. Y. Glebov, P. B. Radha, C. Stoeckl, S. Roberts, C. Sorce, T. C. Sangster, M. D. Cable, K. Fletcher, and S. Padalino, Physics of Plasmas **9**, 2725 (2002).
[23] S. Kurebayashi, J. A. Frenje, F. H. Séguin, J. R. Rygg, C. K. Li, R. D. Petrasso, V. Y. Glebov, J. A. Delettrez, T. C. Sangster, D. D. Meyerhofer, C. Stoeckl, J. M. Soures, P. A. Amendt, S. P. Hatchett, and R. E. Turner, Physics of Plasmas **12**, 032703 (2005).
[24] P. B. Radha, J. Delettrez, R. Epstein, V. Yu Glebov, R. Keck, R. L. McCrory, P. McKenty, D. D. Meyerhofer, F. Marshall, S. P. Regan, S. Roberts, T. C. Sangster, W. Seka, S. Skupsky, V. Smalyuk, C. Sorce, C. Stoeckl, J. Soures, R. P. J. Town, B. Yaakobi, J. Frenje, C. K. Li, R. Petrasso, F. Seguin, K. Fletcher, S. Padalino, C. Freeman, N. Izumi, R. Lerche, and T. W. Phillips, Physics of Plasmas **9**, 2208 (2002).
[25] T. R. Boehly, D. L. Brown, R. S. Craxton, R. L. Keck, J. P. Knauer, J. H. Kelly, T. J. Kessler, S. A. Kumpan, S. J. Loucks, S. A. Letzring, F. J. Marshall, R. L. McCrory, S. F. B. Morse, W. Seka, J. M. Soures, and C. P. Verdon, Optics Communications **133**, 495 (1997).
[26] J. R. Rygg, J. A. Frenje, C. K. Li, F. H. Séguin, R. D. Petrasso, D. D. Meyerhofer, and C. Stoeckl, Phys. Rev. E **80**, 026403 (2009), 10.1103/PhysRevE.80.026403.
[27] H. G. Rinderknecht, M. J. Rosenberg, C. K. Li, N. M. Hoffman, G. Kagan, A. B. Zylstra, H. Sio, J. A. Frenje, M. Gatu Johnson, F. H. Séguin, R. D. Petrasso, P. Amendt, C. Bellei, S. Wilks, J. Delettrez, V. Y. Glebov, C. Stoeckl, T. C. Sangster, D. D. Meyerhofer, and A. Nikroo, Physical Review Letters **114**, 025001 (2015).
[28] C.-K. Li and R. D. Petrasso, Physical Review Letters **70**, 3059 (1993).
[29] C.-K. Li and R. D. Petrasso, Phys. Rev. Lett. **114**, 199901 (2015), 10.1103/PhysRevLett.114.199901.

[30] Here and throughout this work, the nuclear production is assumed to occur volumetrically in a spherically symmetric plasma.
[31] Deuterium areal density, $\rho R_d = n_d m_d R$, is the areal density value relevant to secondary yield production – effectively, how many deuterons the reactant particle 'sees' in-flight – while the total areal density in the fuel ρR_{total} is relevant for stopping power. In Figure 3a) the plasma is pure deuterium so $\rho R_d = \rho R_{total}$. In Figure 3b) the horizontal shift between the curves is set almost entirely by the scaling factor $\rho R_d = (f_d A_d / \langle A \rangle) \rho R_{total}$, where $\langle A \rangle$ is the average ion mass in the plasma.
[32] For the T=10 keV scenario, the ^{3}He ions that stop in the plasma

lose only ∼42% of their energy to the electrons and the remaining ∼58% to the deuterons; likewise, the tritons lose ∼47% to the electrons and ∼53% to the deuterons. Although the stopping on ions is not discussed analytically in this work, it is incorporated into the combined secondary yield analysis calculations.

[33]F. H. Séguin, N. Sinenian, M. Rosenberg, A. Zylstra, M. J.-E. Manuel, H. Sio, C. Waugh, H. G. Rinderknecht, M. G. Johnson, J. Frenje, C. K. Li, R. Petrasso, T. C. Sangster, and S. Roberts, Review of Scientific Instruments **83**, 10D908 (2012).

[34]A. Zylstra, *Using fusion-product spectroscopy to study inertial fusion implosions, stopping power, and astrophysical nucleosynthesis at OMEGA and the NIF*, Ph.D. thesis, Massachusetts Institute of Technology (2015).

[35]G. B. Zimmerman, "Recent Developments in Monte Carlo Techniques," Tech. Rep. UCRL-JC-105616 (Lawrence Livermore National Laboratory, 1990).

[36]G. Maynard and C. Deutsch, Phys. Rev. A **26**, 665 (1982).

[37]F also depends on the shape of the stopping power curve. However, since the temperature is fixed in this formalism and stopping on the ions is neglected, the shape of the stopping power curve does not change aside from an amplitude scaling with the electron density, which has already been removed.

[38]J. D. Lindl, P. Amendt, R. L. Berger, S. G. Glendinning, S. H. Glenzer, S. W. Haan, R. L. Kauffman, O. L. Landen, and L. J. Suter, Physics of Plasmas **11**, 339 (2004).

[39]C. K. Li, F. H. Séguin, J. A. Frenje, J. R. Rygg, R. D. Petrasso, R. P. J. Town, P. A. Amendt, S. P. Hatchett, O. L. Landen, A. J. Mackinnon, P. K. Patel, V. A. Smalyuk, J. P. Knauer, T. C. Sangster, and C. Stoeckl, Review of Scientific Instruments **77**, 10E725 (2006).

[40]J. R. Rygg, J. A. Frenje, C. K. Li, F. H. Séguin, R. D. Petrasso, J. A. Delettrez, V. Y. Glebov, V. N. Goncharov, D. D. Meyerhofer, S. P. Regan, T. C. Sangster, and C. Stoeckl, Physics of Plasmas **13**, 052702 (2006).

[41]M. J. Rosenberg, H. G. Rinderknecht, N. M. Hoffman, P. A. Amendt, S. Atzeni, A. B. Zylstra, C. K. Li, F. H. Séguin, H. Sio, M. G. Johnson, J. A. Frenje, R. D. Petrasso, V. Y. Glebov, C. Stoeckl, W. Seka, F. J. Marshall, J. A. Delettrez, T. C. Sangster, R. Betti, V. N. Goncharov, D. D. Meyerhofer, S. Skupsky, C. Bellei, J. Pino, S. C. Wilks, G. Kagan, K. Molvig, and A. Nikroo, Physical Review Letters **112**, 185001 (2014).

[42]A. B. Zylstra, J. A. Frenje, F. H. Séguin, D. G. Hicks, E. L. Dewald, H. F. Robey, J. R. Rygg, N. B. Meezan, M. J. Rosenberg, H. G. Rinderknecht, S. Friedrich, R. Bionta, R. Olson, J. Atherton, M. Barrios, P. Bell, R. Benedetti, L. Berzak Hopkins, R. Betti, D. Bradley, D. Callahan, D. Casey, G. Collins, S. Dixit, T. Döppner, D. Edgell, M. J. Edwards, M. Gatu Johnson, S. Glenn, S. Glenzer, G. Grim, S. Hatchett, O. Jones, S. Khan, J. Kilkenny, J. Kline, J. Knauer, A. Kritcher, G. Kyrala, O. Landen, S. LePape, C. K. Li, J. Lindl, T. Ma, A. Mackinnon, A. Macphee, M. J.-E. Manuel, D. Meyerhofer, J. Moody, E. Moses, S. R. Nagel, A. Nikroo, A. Pak, T. Parham, R. D. Petrasso, R. Prasad, J. Ralph, M. Rosen, J. S. Ross, T. C. Sangster, S. Sepke, N. Sinenian, H. W. Sio, B. Spears, P. Springer, R. Tommasini, R. Town, S. Weber, D. Wilson, and R. Zacharias, Physics of Plasmas **21**, 112701 (2014).

[43]V. Y. Glebov, C. Stoeckl, T. C. Sangster, S. Roberts, G. J. Schmid, R. A. Lerche, and M. J. Moran, Review of Scientific Instruments **75**, 3559 (2004).

[44]V. Y. Glebov, T. C. Sangster, C. Stoeckl, J. P. Knauer, W. Theobald, K. L. Marshall, M. J. Shoup, T. Buczek, M. Cruz, T. Duffy, M. Romanofsky, M. Fox, A. Pruyne, M. J. Moran, R. A. Lerche, J. McNaney, J. D. Kilkenny, M. J. Eckart, D. Schneider, D. Munro, W. Stoeffl, R. Zacharias, J. J. Haslam, T. Clancy, M. Yeoman, D. Warwas, C. J. Horsfield, J.-L. Bourgade, O. Landoas, L. Disdier, G. A. Chandler, and R. J. Leeper, Review of Scientific Instruments **81**, 10D325 (2010).

[45]M. J. Rosenberg, A. B. Zylstra, F. H. Séguin, H. G. Rinderknecht, J. A. Frenje, M. Gatu Johnson, H. Sio, C. J. Waugh, N. Sinenian, C. K. Li, R. D. Petrasso, P. W. McKenty, M. Hohenberger, P. B. Radha, J. A. Delettrez, V. Y. Glebov, R. Betti, V. N. Goncharov, J. P. Knauer, T. C. Sangster, S. LePape, A. J. Mackinnon, J. Pino, J. M. McNaney, J. R. Rygg, P. A. Amendt, C. Bellei, L. R. Benedetti, L. Berzak Hopkins, R. M. Bionta, D. T. Casey, L. Divol, M. J. Edwards, S. Glenn, S. H. Glenzer, D. G. Hicks, J. R. Kimbrough, O. L. Landen, J. D. Lindl, T. Ma, A. MacPhee, N. B. Meezan, J. D. Moody, M. J. Moran, H.-S. Park, B. A. Remington, H. Robey, M. D. Rosen, S. C. Wilks, R. A. Zacharias, H. W. Herrmann, N. M. Hoffman, G. A. Kyrala, R. J. Leeper, R. E. Olson, J. D. Kilkenny, and A. Nikroo, Physics of Plasmas (1994-present) **21**, 122712 (2014), 10.1063/1.4905064.

[46]This calculation, performed in reverse, is used to determine the convergence ratio in the experiment.

[47]J. Delettrez, R. Epstein, M. C. Richardson, P. A. Jaanimagi, and B. L. Henke, Phys. Rev. A **36**, 3926 (1987).

[48]M. J. Rosenberg, F. H. Séguin, P. A. Amendt, S. Atzeni, H. G. Rinderknecht, N. M. Hoffman, A. B. Zylstra, C. K. Li, H. Sio, M. G. Johnson, J. A. Frenje, R. D. Petrasso, V. Y. Glebov, C. Stoeckl, W. Seka, F. J. Marshall, B. Yaakobi, J. A. Delettrez, T. C. Sangster, R. Betti, C. Bellei, J. Pino, S. C. Wilks, K. Molvig, and A. Nikroo, Physics of Plasmas (in preparation).

[49]S. Le Pape, L. Divol, L. Berzak Hopkins, A. Mackinnon, N. B. Meezan, D. Casey, J. Frenje, H. Herrmann, J. McNaney, T. Ma, K. Widmann, A. Pak, G. Grimm, J. Knauer, R. Petrasso, A. Zylstra, H. Rinderknecht, M. Rosenberg, M. Gatu-Johnson, and J. D. Kilkenny, Physical Review Letters **112**, 225002 (2014).

[50]J. D. Huba, "NRL Plasma Formulary," (online), Naval Research Laboratory, Washington, D.C. (2006).

[51]A. J. MacKinnon, N. B. Meezan, J. S. Ross, S. Le Pape, L. Berzak Hopkins, L. Divol, D. Ho, J. Milovich, A. Pak, J. Ralph, T. Döppner, P. K. Patel, C. Thomas, R. Tommasini, S. Haan, A. G. MacPhee, J. McNaney, J. Caggiano, R. Hatarik, R. Bionta, T. Ma, B. Spears, J. R. Rygg, L. R. Benedetti, R. P. J. Town, D. K. Bradley, E. L. Dewald, D. Fittinghoff, O. S. Jones, H. R. Robey, J. D. Moody, S. Khan, D. A. Callahan, A. Hamza, J. Biener, P. M. Celliers, D. G. Braun, D. J. Erskine, S. T. Prisbrey, R. J. Wallace, B. Kozioziemski, R. Dylla-Spears, J. Sater, G. Collins, E. Storm, W. Hsing, O. Landen, J. L. Atherton, J. D. Lindl, M. J. Edwards, J. A. Frenje, M. Gatu-Johnson, C. K. Li, R. Petrasso, H. Rinderknecht, M. Rosenberg, F. H. Séguin, A. Zylstra, J. P. Knauer, G. Grim, N. Guler, F. Merrill, R. Olson, G. A. Kyrala, J. D. Kilkenny, A. Nikroo, K. Moreno, D. E. Hoover, C. Wild, and E. Werner, Physics of Plasmas (1994-present) **21**, 056318 (2014), 10.1063/1.4876611.

[52]S. Skupsky, J. A. Marozas, R. S. Craxton, R. Betti, T. J. B. Collins, J. A. Delettrez, V. N. Goncharov, P. W. McKenty, P. B. Radha, T. R. Boehly, J. P. Knauer, F. J. Marshall, D. R. Harding, J. D. Kilkenny, D. D. Meyerhofer, T. C. Sangster, and R. L. McCrory, Physics of Plasmas (1994-present) **11**, 2763 (2004), 10.1063/1.1689665.

[53]M. J. Schmitt, P. A. Bradley, J. A. Cobble, J. R. Fincke, P. Hakel, S. C. Hsu, N. S. Krasheninnikova, G. A. Kyrala, G. R. Magelssen, D. S. Montgomery, T. J. Murphy, K. A. Obrey, R. C. Shah, I. L. Tregillis, J. A. Baumgaertel, F. J. Wysocki, S. H. Batha, R. Stephen Craxton, P. W. McKenty, P. Fitzsimmons, A. Nikroo, and R. Wallace, Physics of Plasmas **20**, 056310 (2013).

[54]T. J. Murphy, G. A. Kyrala, N. S. Krasheninnikova, P. A. Bradley, J. A. Cobble, I. L. Tregillis, K. A. D. Obrey, J. A. Baumgaertel, S. C. Hsu, R. C. Shah, P. Hakel, J. L. Kline, M. J. Schmitt, R. J. Kanzleiter, S. H. Batha, R. J. Wallace, S. Bhandarkar, P. Fitzsimmons, M. Hoppe, A. Nikroo., and P. McKenty, Journal of Physics: Conference Series **(accepted)** (2015).

[55]N. Izumi, T. Ma, M. Barrios, L. R. Benedetti, D. Callahan, C. Cerjan, J. Edwards, S. Glenn, S. Glenzer, J. Kilkenny, J. Kline, G. Kyrala, O. L. Landen, S. Regan, P. Springer, L. Suter, R. Tommasini, R. Town, A. J. Mackinnon, P. Bell, and D. K. Bradley, Review of Scientific Instruments **83**, 10E121 (2012), 10.1063/1.4738660.

[56]P. Scott, "Chi-Square: Testing for Goodness of Fit," see `http://physics.ucsc.edu/~drip/133.html` (2000), Intermediate Lab

Manual, Chapter 4.

[57]H. Brysk, Plasma Physics **15**, 611 (1973).